Accurate and efficient structure factors in ultrasoft pseudopotential and projector augmented wave DFT

Benjamin X. Shi [●],[*] Rebecca J. Nicholls, and Jonathan R. Yates [●][†]
Department of Materials, University of Oxford, Parks Road, Oxford OX1 3PH, United Kingdom

Structure factors obtained from diffraction experiments are one of the most important quantities for characterizing the electronic and structural properties of materials. Methods for calculating this quantity from plane-wave density functional theory (DFT) codes are typically prohibitively expensive to perform, requiring the electron density to be constructed and evaluated on dense real-space grids. Making use of the projector functions found in both the Vanderbilt ultrasoft pseudopotential and projector augmented wave methods, we implement an approach to calculate structure factors that avoids the use of a dense grid by separating the rapidly changing contributions to the electron density and treating them on logarithmic radial grids. This approach is successfully validated against structure factors obtained from all-electron DFT and experiment for three prototype systems, allowing structure factors to be obtained at all-electron accuracy at a fraction of the cost of previous approaches for plane-wave DFT.

I. INTRODUCTION

The structure factor (SF) is a fundamentally important quantity in the physical and biological sciences. Experimental SFs have become the principal tool for characterizing the geometrical structure (e.g., atomic positions and elements) of a range of crystalline matter, from simple materials [1] to complex biomolecules [2]. Beyond structural information, the (x-ray) SFs are the Fourier coefficients of the electron density (ED), $n(\mathbf{r})$, and allow for its reconstruction through an inverse Fourier transform [3]. The ED contains a wealth of information, as established by the Hohenberg-Kohn theorems [4], which states that the ground-state electronic properties of a system are a unique functional of the ground-state ED. Reconstructed EDs have been used to investigate the properties of a range of materials, from the anisotropic elastic constants of Al [5] to the electronic origins of high-temperature cuprate superconductors [6,7].

Accurate SFs calculated from first-principles methods, particularly density functional theory (DFT), are necessary for the above applications of SFs. For example, SFs computed from DFT have been used to augment experimental SFs to allow full reconstruction of the ED. By themselves, SFs obtained from x-ray [7–9], γ-ray [10–12], or electron-diffraction

[13–16] experiments can only provide a finite set of SFs, introducing Fourier series truncation errors to the reconstructed ED [17] if used alone. Many of these diffraction experiments are also incapable of obtaining the phase of the complex SFs in noncentrosymmetric crystals—the phase problem [18]. DFT helps to alleviate these problems as it can generate many SFs to augment those that are not provided by experiments while also providing phase information. The SFs from DFT are also used to assess the quality of experimental diffraction techniques. For example, extinction effects [19,20] and the x-ray source [21] can affect measurements in x-ray diffraction experiments. In electron diffraction, material preparation [22] and instrument distortions [23] can serve as potential error sources.

Likewise, high-precision SFs from experiments can also help validate the approximations used in DFT [14,24–26]. Based upon the Hohenberg-Kohn theorems, practical DFT calculations attempt to approximate the exact energy functional, which is unknown, to the ED through density functional approximations (DFAs). There is a whole "zoo" [27] of available DFAs, with no systematic manner to determine their accuracy. There has been some evidence [28] to show that modern DFT may be giving improved energetic descriptions of (atomic) systems at the cost of a worse ED. This has motivated increased interest in benchmarking the ED of DFAs, with high-precision SFs obtained from diffraction being one of the few experiments that can achieve this.

Beyond just accuracy, it is also highly desirable that SFs can be obtained from DFT *efficiently* without incurring heavy computational burden or time to allow for more complex systems to be tackled. Unfortunately, current approaches to calculate the SF from DFT methods are not efficient, requiring a high computational cost. The SF calculation is a postprocessing step that converts the ED taken from either all-electron (AE) or plane-wave pseudopotential (PP) DFT methods. AE

---

*Present address: Yusuf Hamied Department of Chemistry, University of Cambridge, Lensfield Road, Cambridge CB2 1EW, United Kingdom.
†jonathan.yates@materials.ox.ac.uk

DFT approaches treat all the electrons in the system explicitly, enabling highly accurate calculations. They are commonly used to compute SFs as these approaches typically decompose the ED into angular components near the nuclei, making subsequent SF calculations easier to perform. However, obtaining the ED comes at significant computational cost due to the $\sim O(N^3)$ [29] scaling of DFT with number of electrons N. The inclusion of a pseudopotential [30] in PP DFT decreases the computational cost for obtaining the ED from DFT as only valence electrons need to be treated. However, the resulting ED only includes the contributions from the valence electrons and has been smoothed (pseudized) near the core.

In PP DFT, the projector augmented wave (PAW) method can provide all-electron properties by adding a compensating augmentation charge (to restore the valence nodes) and adding the frozen (atomic) core ED. Beyond its original derivation [31,32] for energies, forces, and the ED, the PAW method has also been derived for other key properties such as electron-phonon interactions [33,34], optical [35–38], NMR [39,40], and x-ray absorption spectra [41–43], etc. Typically, applying the PAW method comes at little additional costs for its added accuracy because quantities that change rapidly are calculated on radial grids around each atom, while smoother quantities are calculated on a real-space grid. However, current approaches of calculating the SF from PAW DFT are expensive because the entire AE total ED is reconstructed on a real-space fast Fourier transform (FFT) grid. This FFT grid has to be very dense (several orders of magnitude denser than default) to have sufficient spatial resolution to accurately capture the rapid oscillations of the AE total ED near the nucleus. As a result, the calculations require a large amount of memory and time, with several studies explicitly highlighting the difficulty with converging the total ED to a sufficient precision due to computational limitations [26,44].

In this paper, we derive expressions to calculate the x-ray structure factor for the PAW method that can also be used in the closely related Vanderbilt ultrasoft pseudopotential [45] method. As such, the developments here are expected to be applicable for virtually all plane-wave PP DFT codes. The major contribution of this implementation is that rapidly changing contributions to the ED are treated separately on radial grids around each atom now. Thus, the FFT grid does not need to be increased beyond its default size, allowing for high computational efficiency. The SFs calculated with this implementation are shown to be highly accurate, as validated against AE DFT and experiment for a range of materials. These comparisons demonstrate that accurate SFs and EDs require appropriately reconstructing both the augmentation charge and frozen core charge densities, necessitating the developments in this work.

II. THE AE ELECTRON DENSITY

This section details how the AE ED is obtained from PP DFT calculations using the Vanderbilt ultrasoft pseudopotential and PAW methods. The theory is applicable for both methods, so unless otherwise stated, PAW DFT will be used to denote both methods hereafter.

In PAW DFT, the AE wave function $\psi_n(\mathbf{r})$ for each of the n valence (Kohn-Sham) orbitals can be reconstructed from its corresponding pseudized (PS) wave function $\tilde{\psi}_n(\mathbf{r})$ through a linear transformation [31]:

$$\psi_n(\mathbf{r}) = \tilde{\psi}_n(\mathbf{r}) + \sum_{\mathbf{R}ju} \left[\phi_u^j(\mathbf{r}_\mathbf{R}^j) - \tilde{\phi}_u^j(\mathbf{r}_\mathbf{R}^j) \right] \langle \tilde{p}_u^j | \tilde{\psi}_n \rangle. \quad (1)$$

Within this expression, $\phi_u^j(\mathbf{r}_\mathbf{R}^j)$ and $\tilde{\phi}_u^j(\mathbf{r}_\mathbf{R}^j)$ are the AE and PS partial waves, respectively, for each atom j in the unit cell, with the projectors $\langle \tilde{p}_u^j |$ designed to be dual to the PS partial waves: $\langle \tilde{p}_u^j | \tilde{\phi}_{u'}^{j'} \rangle = \delta_{jj'}\delta_{uu'}$. The AE partial waves are a set of wave functions obtained from the corresponding reference atom [46], where u is the composite index for the angular momentum quantum numbers l, m as well as an index k to label partial waves constructed at different reference energies [31]. The vectors

$$\mathbf{r}_\mathbf{R}^j = \mathbf{r} - \mathbf{r}_j - \mathbf{R} \quad (2)$$

are used to denote the spatial dependence of the partial waves and projectors to emphasize that these functions are atom centered. These equations assume a periodic material, where $\mathbf{R}$ is the (infinite) set of lattice vectors and $\mathbf{r}_j$ denotes the position of atom j in the unit cell. Computationally, the partial waves and projectors can be expressed as a radial function (stored on logarithmic radial grids) multiplied by a spherical harmonic:

$$\phi_u(\mathbf{r}) = R_{lk}(r)Y_{lm}(\hat{\mathbf{r}}), \quad (3)$$

with the PS partial waves differing from the AE partial waves only within a cutoff r_c^l, where its radial component has been pseudized. The reconstructed wave function in Eq. (1) requires only a limited set of partial waves to match a full AE DFT calculation [47].

The AE valence ED $n_{\text{val}}(\mathbf{r})$ can be given as a sum of two contributions:

$$n_{\text{val}}(\mathbf{r}) = \tilde{n}_{\text{val}}(\mathbf{r}) + n_{\text{aug}}(\mathbf{r}). \quad (4)$$

The first term is the PS valence ED, which is the ED resulting from the PS (valence) wave functions in Eq. (1):

$$\tilde{n}_{\text{val}}(\mathbf{r}) = \sum_n f_n |\tilde{\psi}_n(\mathbf{r})|^2, \quad (5)$$

where f_n are the occupation numbers. The FFT grid is designed to store this smooth function, with its default size sufficient to sample and represent it fully. The second term is the augmentation charge, which restores the PS valence ED to the AE valence ED, taking the form

$$n_{\text{aug}}(\mathbf{r}) = \sum_{\mathbf{R}ju_1u_2} \rho_{u_1u_2}^j Q_{u_1u_2}^j(\mathbf{r}_\mathbf{R}^j). \quad (6)$$

The augmentation functions $Q_{u_1u_2}^j(\mathbf{r}_\mathbf{R}^j)$ are defined as

$$Q_{u_1u_2}^j(\mathbf{r}) = \phi_{u_1}^j(\mathbf{r})^* \phi_{u_2}^j(\mathbf{r}) - \tilde{\phi}_{u_1}^j(\mathbf{r})^* \tilde{\phi}_{u_2}^j(\mathbf{r}), \quad (7)$$

where u_1 and u_2 are two sets of u indices, with $\rho_{u_1u_2}^j$ giving the occupancy of each u_1, u_2 augmentation function channel for atom j:

$$\rho_{u_1u_2}^j = \sum_n f_n \langle \tilde{\psi}_n | \tilde{p}_{u_1}^j \rangle \langle \tilde{p}_{u_2}^j | \tilde{\psi}_n \rangle. \quad (8)$$

The augmentation function $Q_{u_1u_2}^j(\mathbf{r})$ will be localized around atom j in an "augmentation" region. The two most common

types of pseudopotentials are the norm-conserving PPs (NCPs) and ultrasoft PPs (USPs). NCPs are constructed to preserve the norm of the wave (i.e., the integral of the augmentation functions within the augmentation region is zero by construction), while USPs relax this condition, requiring fewer plane waves to describe the PS valence wave functions at the cost of additional complexity. It is standard practice when using NCPs to neglect any augmentation to the charge density during the calculation of the ground state. Following from Eqs. (3) and (7), $Q_{u_1 u_2}^j(\mathbf{r})$ can be expressed as the product of a radial function $\Delta R_{u_1 u_2}^j(r)$ and two spherical harmonics:

$$Q_{u_1 u_2}^j(\mathbf{r}) = \Delta R_{u_1 u_2}^j(r) Y_{l_1 m_1}^*(\hat{\mathbf{r}}) Y_{l_2 m_2}(\hat{\mathbf{r}}). \qquad (9)$$

Within the PAW method, the radial functions in the augmentation functions are treated on atom-centered logarithmic radial support grids [32], with the spherical harmonics treated analytically, while in the Vanderbilt ultrasoft pseudopotential approach, these functions are typically pseudized and placed onto the FFT grid [48]. While this pseudization gives accurate total energies [49], the use of a PS compared to the AE augmentation charge introduces significant errors in the calculations of SF, as will be shown in Sec. IV.

The PAW method typically utilizes the frozen core approximation. Under this scheme, the core ED is a superposition of the core EDs ρ_{core}^j obtained from isolated atoms:

$$n_{core}(\mathbf{r}) = \sum_{\mathbf{R} j} \rho_{core}^j(|\mathbf{r}_{\mathbf{R}}^j|). \qquad (10)$$

These atomic core EDs are spherically symmetric and obtained from solving the radial Kohn-Sham Schrödinger equation [46] on the logarithmic radial support grids.

Overall, the total AE ED will then be the sum of the PS valence, augmentation charge, and frozen core EDs:

$$n(\mathbf{r}) = \tilde{n}_{val}(\mathbf{r}) + n_{aug}(\mathbf{r}) + n_{core}(\mathbf{r}). \qquad (11)$$

III. THE AE STRUCTURE FACTORS

This section details how the AE SFs can be obtained from the AE ED in PAW DFT codes. The AE SFs $F(\mathbf{H})$ are the Fourier coefficients of the AE (total) ED:

$$F(\mathbf{H}) = \mathcal{F}[n(\mathbf{r})], \qquad (12)$$

where $\mathbf{H} = h\mathbf{a}^* + k\mathbf{b}^* + l\mathbf{c}^*$ is the scattering vector corresponding to the (hkl) plane and the crystallographic convention for the primitive reciprocal lattice vectors $\mathbf{a}^*$, $\mathbf{b}^*$, and $\mathbf{c}^*$ has been used. Current methods of obtaining the AE SFs from the AE ED in PAW DFT codes involves constructing the AE ED onto a uniform grid before applying a fast Fourier transform (FFT). This approach is highly inefficient because the FFT grid used has to be several orders of magnitude denser than the default (designed for the PS valence ED only) to accommodate the rapidly varying augmentation and core charges near the nuclei. As shown in Fig. S1 of the Supplemental Material [50], this leads to orders of magnitude increases in time and peak random access memory. The impact of the resulting additional computational burden has been noted in previous studies [26].

In this section, we propose and derive an approach to calculate AE SFs efficiently and accurately in the PAW DFT

method. It works by separating the three individual contributions to the AE total ED from PAW DFT and treating the two terms that require high spatial resolution near the nuclei: n_{aug} and n_{core}, on logarithmic radial support grids and analytically for radial and angular components, respectively. These radial grids are one-dimensional with a high density of points placed near the nuclei to achieve high accuracy efficiently.

From the linearity principle of the Fourier transform, the SF can be separated into three contributions:

$$F(\mathbf{H}) = \tilde{F}_{val}(\mathbf{H}) + F_{core}(\mathbf{H}) + F_{aug}(\mathbf{H}), \qquad (13)$$

where $\tilde{F}_{val}(\mathbf{H})$, $F_{core}(\mathbf{H})$, and $F_{aug}(\mathbf{H})$ are the Fourier transforms of $\tilde{n}_{val}(\mathbf{r})$, $n_{core}(\mathbf{r})$, and $n_{aug}(\mathbf{r})$, respectively. By nature, $\tilde{n}_{val}(\mathbf{r})$ is constructed to be fully described on the coarse (default) FFT grid size. Thus, its Fourier transform can be computed efficiently using the FFT method, a fundamental component of all plane-wave DFT codes.

The theory for treating the core and augmentation contributions to the SF in the next two sections relies on some of the methods developed for the independent atom model (IAM), commonly used in crystallography. The IAM is constructed as a summation of isolated atomic densities $\rho^j(\mathbf{r})$ about their atomic positions:

$$n_{IAM}(\mathbf{r}) = \sum_{\mathbf{R} j} \rho^j(\mathbf{r}_{\mathbf{R}}^j), \qquad (14)$$

and it is possible to show that its SF takes the form [3]

$$F_{IAM}(\mathbf{H}) = \sum_j f^j(\mathbf{H}) \exp(i2\pi \mathbf{H} \cdot \mathbf{r}_j), \qquad (15)$$

where $f^j(\mathbf{H})$ is the atomic scattering factor, defined to be the Fourier transform of the corresponding $\rho^j(\mathbf{r})$:

$$f^j(\mathbf{H}) = \int \rho^j(\mathbf{r}) \exp(i2\pi \mathbf{H} \cdot \mathbf{r}) d\mathbf{r}. \qquad (16)$$

A. Core contribution

Recalling Eq. (10), the core ED is a summation of atom-centered densities, much like the IAM. Thus, using the SF expressions derived for the IAM, the SF contribution from the core ED takes the form

$$F_{core}(\mathbf{H}) = \sum_j f_{core}^j(\mathbf{H}) \exp(i2\pi \mathbf{H} \cdot \mathbf{r}_j), \qquad (17)$$

where the atomic core scattering factor $f_{core}^j(\mathbf{H})$ is the Fourier transform of the corresponding $\rho_{core}^j(\mathbf{r})$:

$$f_{core}^j(\mathbf{H}) = \int \rho_{core}^j(|\mathbf{r}|) \exp(i2\pi \mathbf{H} \cdot \mathbf{r}) d\mathbf{r}. \qquad (18)$$

As $\rho_{core}(|\mathbf{r}|)$ is a spherically symmetric function about the origin, it is more convenient to use the spherical polar coordinate system. Within this coordinate system, the plane-wave function can be expanded into complex spherical harmonic functions [51]:

$$\exp(i2\pi \mathbf{H} \cdot \mathbf{r}) = 4\pi \sum_{l=0}^{\infty} \sum_{m=-l}^{l} i^l j_l(2\pi H r) Y_{l,m}(\hat{\mathbf{H}}) Y_{l,m}^*(\hat{\mathbf{r}}),$$

$$(19)$$

where $j_l(r)$ is the spherical Bessel function of order l. Substituting Eq. (19) into Eq. (18) would then yield

$$f_{\text{core}}^j(H) = \int \rho_{\text{core}}^j(r) 4\pi r^2 j_0(2\pi Hr) dr, \qquad (20)$$

as only the $l = 0$ terms persist due to the rotational invariance of $\rho_{\text{core}}^j(r)$ [and in turn $f_{\text{core}}^j(H)$]. This equation can be evaluated on the native logarithmic radial grids for each atom j within the unit cell and as a result, the core contribution to the SF no longer needs to be evaluated on the FFT grid.

B. Augmentation contribution

Like the core ED and IAM, the augmentation charge also consists of a summation of atom-centered functions, so it can be written to take the form

$$F_{\text{aug}}(\mathbf{H}) = \sum_j \exp(i2\pi\mathbf{H} \cdot \mathbf{r}_j) \sum_{u_1 u_2} f_{u_1 u_2}^j(\mathbf{H}), \qquad (21)$$

where

$$f_{u_1 u_2}^j(\mathbf{H}) = \rho_{u_1 u_2}^j \int Q_{u_1 u_2}^j(\mathbf{r}) \exp(i2\pi\mathbf{H} \cdot \mathbf{r}) d\mathbf{r}. \qquad (22)$$

The augmentation charge differs from the core ED in that these atom-centered functions $Q_{u_1 u_2}^j(\mathbf{r})$ are not spherically symmetric about the origin, instead being expressed as a multiple of a radial function and two spherical harmonics [see Eq. (9)]. The spherical harmonics form a complete set, so their products can be expressed as an expansion of single spherical harmonics:

$$Y_{l_1 m_1}^*(\hat{\mathbf{r}}) Y_{l_2 m_2}(\hat{\mathbf{r}}) = \sum_L C_{l_1 l_2 L}^{m_1 m_2} Y_{LM}(\hat{\mathbf{r}}), \qquad (23)$$

where $M = -m_1 + m_2$, $|l_1 - l_2| \leqslant L \leqslant l_1 + l_2$, and $C_{l_1 l_2 L}^{m_1 m_2}$ are the Clebsch-Gordan coefficients. The augmentation functions $Q_{u_1 u_2}^j(\mathbf{r})$ can then be rewritten as

$$Q_{u_1 u_2}^j(\mathbf{r}) = \Delta R_{u_1 u_2}^j(r) \sum_L C_{l_1 l_2 L}^{m_1 m_2} Y_{LM}(\hat{\mathbf{r}}). \qquad (24)$$

When this new formulation of $Q_{u_1 u_2}^j(\mathbf{r})$ is substituted into Eq. (22), $f_{u_1 u_2}^j(\mathbf{H})$ can be further simplified to

$$f_{u_1 u_2}^j(\mathbf{H}) = \rho_{u_1 u_2}^j \sum_L C_{l_1 l_2 L}^{m_1 m_2} Y_{LM}(\hat{\mathbf{H}}) 4\pi i^L$$
$$\times \int j_L(2\pi Hr) \Delta R_{u_1 u_2}^j(r) r^2 dr, \qquad (25)$$

where the expansion of the plane wave in spherical harmonics [Eq. (19)] and subsequently the orthonormal properties of complex spherical harmonics have been used to arrive at the final expression. Within Eq. (25), the $\int j_L(2\pi Hr) \Delta R_{u_1 u_2}^j(r) r^2 dr$ integral can be evaluated to high precision on the logarithmic radial support grids, while the angular components are treated analytically using spherical harmonics, removing the need to evaluate the augmentation contribution on the FFT grid.

With the method outlined in this section, only the default FFT grid size has to be used to evaluate converged AE SFs in PAW DFT since it only houses the PS valence ED, with the other terms being evaluated efficiently on radial support grids,

resulting in orders of magnitude savings in computational cost (see Fig. S1 of the Supplemental Material [50]).

IV. VALIDATION AGAINST AE DFT

To ensure that the approach outlined in Sec. III is accurate, we have compared the SFs produced via this approach in PAW DFT against AE DFT calculations for the same DFA for three prototypical systems.

A. Computational details

The approach was implemented in CASTEP [52], which is a plane-wave PP DFT code that can use either NCP or USP for ground-state calculations and the PAW method as a post-processing approach to calculate properties such as hyperfine tensors, NMR properties [40], and now SFs (available as of version 22.1). We refer to AE SFs obtained from using this full approach (with augmentation charges treated on radial support grids) as AE-USP or AE-NCP depending on the class of PP used. To investigate the importance of using the full valence ED, results will also be presented for what we shall refer to as the PS-USP and PS-NCP approaches. The PS-NCP approach uses the pseudized valence ED and the ED from the core electrons, without any augmentation charge. The PS-USP also includes the contribution from the pseudized augmentation charge evaluated on the same FFT grid as the valence ED. Details of the pseudopotentials used are given in Sec. S4 of the Supplemental Material [50], with all input parameters and output files from this work made available online (see [73,74]).

The AE DFT SF calculations are performed using the WIEN2K code [53], which uses an augmented plane wave + local orbital (APW+lo) basis set. Here, the wave function and ED in a unit cell are partitioned into spherical muffin tins (MTs) around nuclei represented by radial functions multiplied by spherical harmonics. The remaining interstitial region is described by plane waves. The rapidly and smoothly changing contributions to the ED are in the muffin tins and interstitial regions, respectively, allowing their contributions to the SF to be treated on appropriate radial and FFT grids. Beyond the APW+lo basis sets, other basis sets are available from other AE DFT codes, such as multiwavelets [54] (in, e.g., MRCHEM [55] and MADNESS [56]) which use adaptive real-space grids to reach basis set convergence systematically.

For both AE and PAW DFT calculations, the energy cutoff ($R_{\text{MT}}K$ for AE DFT) and number of k points were varied to ensure that the SFs were numerically converged to 0.001 (e)lectrons, the limits of experimental accuracy. SFs were compared for both the LDA and PBE DFAs in three materials that highlight different bonding and unit cell systems: diamond Si (covalent), hcp Mg (metallic), and rocksalt MgO (ionic). In each system, the amplitudes of SFs with scattering length $\mathbf{s} = |\mathbf{H}|/2$ below 1.5 Å^{-1} were analyzed, removing any SFs that have equivalent amplitudes due to symmetry or under Friedel's law [57]. All forbidden reflections, under the spherical IAM, were also removed, except for the (222) reflection in Si as it has a noticeable amplitude due to the asphericity of the atoms [58]. The R factor is used to assess
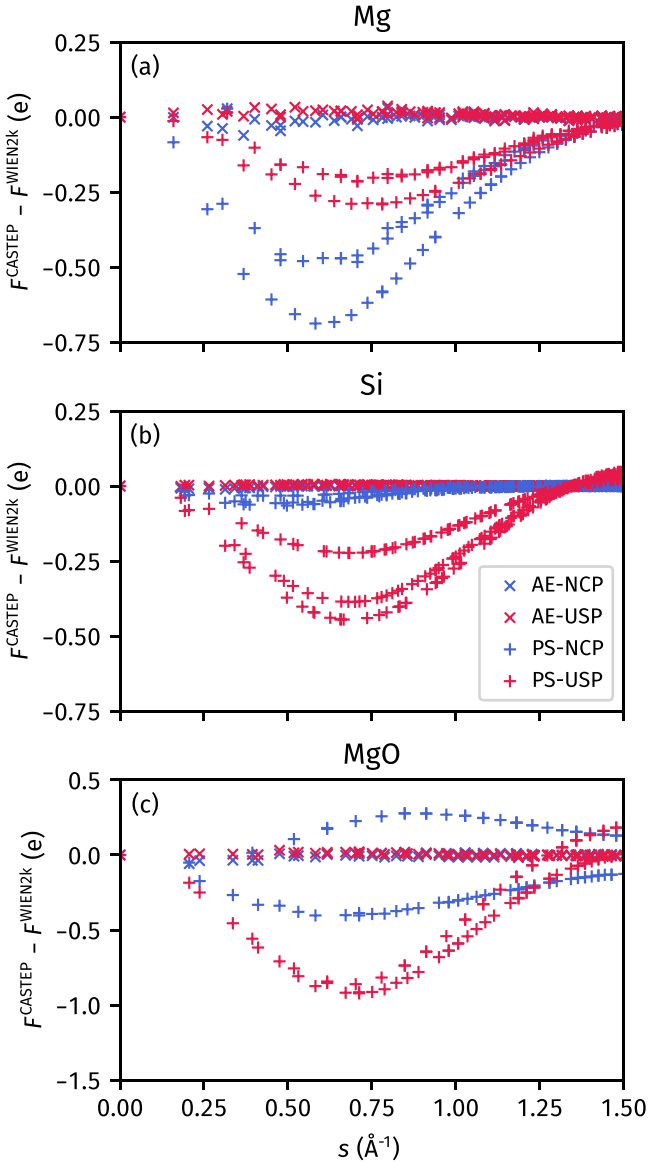
FIG. 1. The difference between APW+lo WIEN2K SF calculations and those obtained from CASTEP as a function of scattering vector s for (a) Si, (b) Mg, and (c) MgO. In CASTEP, PAW DFT calculations were performed employing both USPs and NCPs, with each either using an all-electron (AE) or pseudized (PS) augmentation charge. The PBE functional was used.

the accuracy of our calculations relative to a reference and is defined as

$$R^{\text{ref.}} = \frac{\sum_{\mathbf{H}} |F^{\text{ref.}}(\mathbf{H}) - F^{\text{calc.}}(\mathbf{H})|}{\sum_{\mathbf{H}} |F^{\text{ref.}}(\mathbf{H})|}, \qquad (26)$$

where the reference will be either WIEN2K calculations in this section or experimental values in the following section.

B. Results and discussion

In Fig. 1, the difference between AE DFT WIEN2K and PAW DFT CASTEP calculations, using AE or PS augmentation charges for both USPs and NCPs, were performed for scattering vectors up to 1.5 Å^{-1} for all three materials systems.

TABLE I. R^{WIEN2K} (%) values for the PAW DFT method employing either the USP or NCP in combination with either all-electron (AE) or pseudized (PS) augmentation charges.

		AE-USP	PS-USP	AE-NCP	PS-NCP
Si	LDA	0.05	0.56	0.04	1.03
	PBE	0.04	0.57	0.04	0.99
Mg	LDA	0.04	3.75	0.02	0.29
	PBE	0.03	3.66	0.02	0.28
MgO	LDA	0.05	3.26	0.08	2.01
	PBE	0.05	3.19	0.08	1.98

These plots were for the PBE DFA as we found that the LDA mirrored the plots (see Fig. S2 of the Supplemental Material [50]), suggesting that the differences arise due to the particular pseudization schemes for the pseudopotentials and augmentation charge, which is independent of DFA. For the two monoatomic systems, we see that in the s range of 0.25–1.25 Å^{-1}, there is a systematic underestimation of the SFs for PAW DFT methods that utilize a PS augmentation charge (e.g., PS-NCP and PS-USP). This underestimation arises because these high Fourier components are removed when the oscillating valence ED is made smooth. The magnitude of this underestimation depends on the exact pseudization schemes employed for the pseudopotentials and augmentation charge (for USP) around each atom. Beyond 1.1 Å^{-1}, the SF contributions from the PS valence ED and PS augmentation charge become less than $0.01e$, so that the SF behavior becomes a reflection of the core ED used by the pseudopotential.

Regardless of the pseudopotential, the deviations resulting from a PS augmentation charge are completely removed when the AE augmentation charge is used. The R^{WIEN2K} (in Table I) lowers by at least an order of magnitude for all studied systems from a R^{WIEN2K} of 0.28–3.75% for PS-USP and PS-NCP to a R^{WIEN2K} of 0.02–0.08% for AE-USP and AE-NCP. The errors of AE-USP and AE-NCP with respect to the APW+lo WIEN2K SF values are small enough that they are of the same order as the experimental errors that can arise in high-quality x-ray diffraction experiments. Thus, SFs from AE-USP and AE-NCP (but not PS-USP or PS-NCP) can be used to compare against experiments, as we have done in Sec. V. In addition, we have also compared the real-space electron density between AE-USP and AE-DFT, finding negligible difference, as shown in Sec. S3 of the Supplemental Material [50].

MgO is the only system studied here that contains more than one type of atomic species. For the PS-NCP calculation, there are two observed behaviors in the SFs, with the (hkl) reflections where h, k, l are all odd overestimating the SFs, while those with h, k, l all even underestimating the SFs. This contrasting behavior arises because these two sets arise from different types of reflections. Using Eq. (20) for an IAM, the structure factors where h, k, l are all odd take the form $4(f_{\text{Mg}} - f_{\text{O}})$, arising from a scattering difference between its ions [3] while those that are all even arise from a constructive summation, $4(f_{\text{Mg}} + f_{\text{O}})$. Thus, the SFs with odd h, k, l become sensitive to the specific pseudopotentials of the two

atoms, and may overestimate if one pseudopotential underestimates its scattering factor more strongly than the other.

V. COMPARISON AGAINST EXPERIMENT

Ultimately, the aim of computing AE SFs from DFT is to use it together with experimental SFs, either to augment the (limited) experimental SFs for better ED reconstructions or to validate the approximations in both experiments and DFT. In this section, we will showcase the strength of our approach for the latter application of AE SFs by comparing DFT with two different DFAs and pseudopotentials against experiment, revealing key insights into the effects of these approximations on the accuracy of the ED.

A. Computational details

X-ray SFs obtained from diffraction experiments are influenced by the thermal vibrations of the atoms within the crystal [57], tending to reduce the intensity of the diffracted beams. Comparison of (static) SFs obtained from DFT requires incorporation of these thermal effects to allow for direct comparison, or alternatively, removal of the thermal effects from experimental numbers.

To a good approximation, the SF is the Fourier transform of the thermally averaged ED $\langle n(\mathbf{r}) \rangle$. Within the IAM, thermal effects can be incorporated into the static SF by multiplying each atomic scattering factor $f_j(\mathbf{H})$ in Eq. (16) by an isotropic harmonic temperature factor $T_j(\mathbf{H})$:

$$F(\mathbf{H}) = \sum_j \exp(i2\pi \mathbf{H} \cdot \mathbf{r}_j) f_j(\mathbf{H}) T_j(\mathbf{H}), \qquad (27)$$

where

$$T_j(\mathbf{H}) = \exp(-B_j |\mathbf{H}|^2 / 4). \qquad (28)$$

The Debye-Waller (DW) factor B_j for atom j can be obtained from either fitting of the static SF to experimental SFs [59,60] or using *ab initio* phonon dispersion curves [61]. The derivation of the temperature factor makes two key assumptions: (i) the nuclei vibrate isotropically about their equilibrium positions and (ii) the atomic densities follow the nuclear motion perfectly. The second assumption requires that the crystal ED can be divided into a summation of atom-centered density terms.

Within PAW DFT, the second assumption can be applied to the core and augmentation charges, but not the PS valence ED, since it is "delocalized" and cannot be assigned to any one atom. For monoatomic systems, this problem is trivial because the temperature factor can be applied to the static structure factor as a whole, but it cannot be performed for systems with more than one atomic species. Likewise, this problem also manifests in the APW+lo AE DFT approach of WIEN2K, where its MTs are localized but the interstitial regions are not. Prior studies using the APW+lo codes have overcome this problem by applying the average DW factor of the atomic species, the average method, to the interstitial region [14,62]; this approximation is sufficient because the interstitial region makes up a small proportion of the total ED. The valence electrons in PAW DFT make up a more significant contribution to the total ED compared to the in-

TABLE II. $R^{\text{expt.}}$ (%) values for the APW+lo AE DFT method and the PAW DFT method employing either the USP or NCP in combination with either AE or PS augmentation charges.

		APW+lo	AE-USP	PS-USP	AE-NCP	PS-NCP
Si	LDA	0.24	0.20	0.71	0.25	1.52
	PBE	0.13	0.13	0.57	0.14	1.33
Mg	LDA	0.48	0.45	2.17	0.53	0.86
	PBE	0.36	0.34	2.03	0.42	0.74
MgO	LDA	0.34	0.32	1.43	0.32	0.58
	PBE	0.32	0.30	1.26	0.35	0.53

terstitial region in APW+lo AE DFT (see Table S1 of the Supplemental Material [50]), such that it may be inaccurate to use an average DW factor. Hence, in this study, we will instead use the Hirshfeld partitioning [63] scheme (see Sec. S5 of the Supplemental Material [50]) to divide the valence electron density into atom-centered densities. This approach is found to give a small improvement over the average method in terms of $R^{\text{expt.}}$ across all functionals and pseudopotentials tested for MgO (see Table S2 of the Supplemental Material [50]). It is expected to give even larger improvements in systems with a large disparity in valence electrons or DW factors where it can account for the relative contributions of the different species.

The SFs with thermal vibrations included through the above scheme was compared to experimental SF for the same three systems as the previous section: Mg [25], Si [24], and MgO [14]. Experimental details can be found in their respective references. Thermal effects had already been removed from the structure factors provided by the experimental study on Mg, so we did not apply a Debye-Waller factor to this system. Compared to theoretical SFs computed from DFT, only a small number of SFs (particularly for Mg and MgO) were available from experiment and only these were compared in the subsequent analysis. To be consistent with the prior experimental and theoretical literature on Si, we will compare the "effective" atomic scattering factor of this system. Its relation to the structure factor is given by

$$f(\mathbf{H}) = f(hkl) = \frac{F(hkl)}{8 \cos\left[\frac{\pi}{4}(h + k + l)\right]}. \qquad (29)$$

This equation was derived for the spherical IAM, which predicts the (222) reflection to be forbidden. However, both DFT and experiment predict noticeable intensity in this reflection due to the asphericity of the ED, so it was included as well, with its *atomic* scattering factor defined as $f(222) = F(222)/8$ to give the relative contribution from each atom of the conventional unit cell [24].

B. Results and discussion

Table II evaluates $R^{\text{expt.}}$ for Si, Mg, and MgO from APW+lo WIEN2K and PAW CASTEP calculations. We have compared PAW results incorporating either AE or PS augmentation charges. For both USPs and NCPs, the use of PS augmentation charges leads to an $R^{\text{expt.}}$ that can be three to five times larger than the AE DFT results. This large $R^{\text{expt.}}$ is particularly caused by a systematic underestimation of
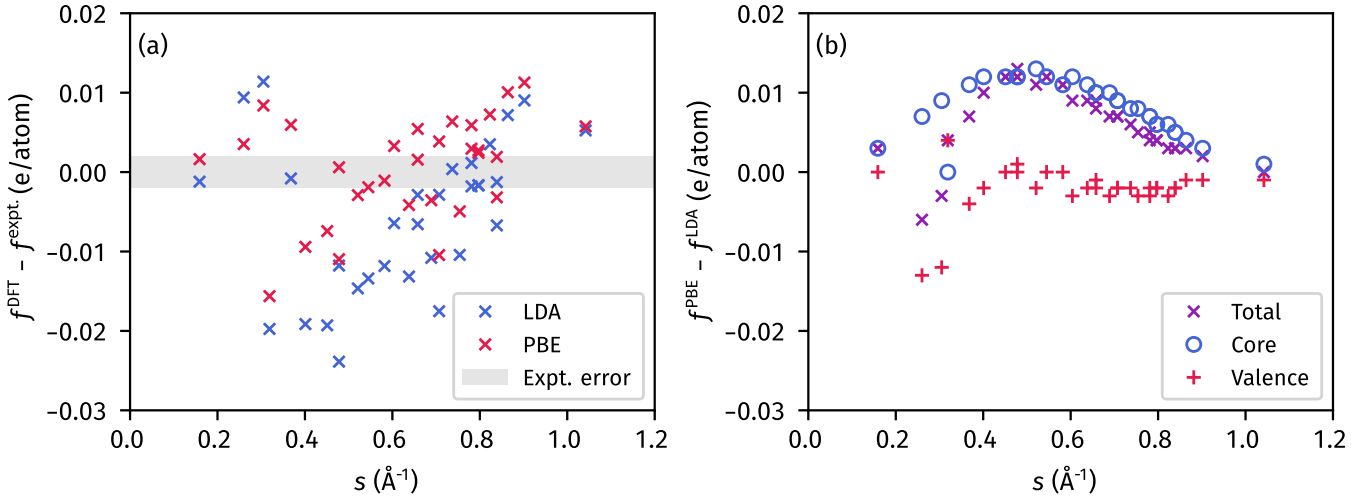
FIG. 2. (a) The difference between experimental atomic scattering factors and those obtained from AE-USP CASTEP as a function of scattering vector s for Si for both the LDA and the PBE density functional approximations (DFAs). (b) The total difference between the atomic scattering factors of the PBE and LDA DFAs and the separation of this difference into its core and valence (including augmentation) contributions.

high Fourier components (see Fig. S4 of the Supplemental Material [50]). When the AE augmentation charge is used, the resulting $R^{expt.}$ are all within 0.06% of the AE DFT results, with the USPs generally performing better than their NCP counterparts. In fact, the USPs even appear to be better than AE DFT by up to 0.04% in $R^{expt.}$ across the three systems and two DFAs. However, this improvement is not statistically significant because each experimentally determined SF has an associated error in its value, which we found to propagate to an error of around ±0.05% in the $R^{expt.}$ for Si.

In Fig. 2(a), the difference in atomic scattering factors for Si between experiment and the AE-USP method from CASTEP is plotted for LDA and PBE. We have focused on Si specifically because there are many available experimental SFs that have been consolidated to high precision from multiple studies. In general, both LDA and PBE underestimates the SFs in the range of $s = 0.4$–0.8 Å^{-1}. The improved $R^{expt.}$ for PBE arises within the 0.4–0.6 Å^{-1} region, where its underestimation of experimental SFs is less, agreeing with the observations of Zuo *et al.* [24].

Compared to APW+lo DFT, where a large portion of the valence electrons is treated in the MT spheres, our approach makes it simple [see Eq. (13)] to obtain the core and valence (PS valence and AE augmentation charge) contributions to the SF; the difference in these two contributions between PBE and LDA is plotted for Si in Fig. 2(b). Below 0.4 Å^{-1}, the valence electrons significantly contribute to the differences in the total scattering factors, but this effect becomes small beyond 0.4 Å^{-1}, which arises because the valence electrons contribute less than 2% to the total scattering factor at that point (see Fig. S5 of the Supplemental Material [50]). Thus, the marked improvement in the 0.4–0.6 Å^{-1} region of PBE over LDA arises predominantly from a better description of the core electrons. This core ED makes up the frozen core in PAW DFT, which, in turn, determines the corresponding pseudopotentials. As it is difficult to construct pseudopotentials for more sophisticated DFAs such as hybrid functionals [64],

the GGA pseudopotential is commonly used instead. Our observations demonstrate that this uncontrolled approximation will make it problematic to compare the ED or SFs of such DFAs since they share the same frozen core ED as the less sophisticated DFA used to generate the pseudopotential, so any analysis will not reflect improvements in the core ED.

VI. CONNECTION TO ELECTRON MICROSCOPY AND THE ELECTRON-SCATTERING FACTOR

In recent years, electron microscopy techniques such as ptychography and scanning transmission electron microscopy have advanced rapidly [65]. The higher accuracy has meant that the commonly used IAM is insufficient, requiring DFT to provide quantitative agreement between simulated microscopy images and experiment.

Simulating electron microscopy images requires the electrostatic potential to be constructed [66]. For PP DFT, it is important that contributions from the core and augmentation charges are incorporated into the electrostatic potential, and several strategies have been devised in recent years. For example, Borghardt *et al.* [67] incorporated a correction in the electrostatic potential near atomic cores from atomic PP and AE DFT calculations whilst Naginey *et al.* [68,69] incorporated a pseudized augmentation charge and frozen core. Both these approaches cannot account for core polarization, which Susi *et al.* [70,71] were able to overcome by utilizing the PAW method to reconstruct the total electrostatic potential in a real-space grid; this required converging the electrostatic and DFT grids alongside further approximations.

X-ray structure factors share a formal relationship with the electron-scattering factor, the Fourier transform of the electrostatic potential, via the Mott-Bethe formula [72]. Thus, in principle, the structure factors produced by our approach can be converted to electron-scattering factors at negligible computational cost and should account for core-polarization effects whilst requiring no grids to converge.

VII. CONCLUSION AND OUTLOOK

We have proposed an efficient approach to obtaining accurate x-ray SFs for the Vanderbilt ultrasoft pseudopotential and projector augmented wave methods within DFT. Compared to prior approaches, involving constructing the total ED on a uniform regular grid, this approach circumvents such a need by evaluating the core and augmentation charges on logarithmic radial support grids, significantly reducing the calculation cost and time. This approach was implemented in CASTEP 22.1 and used to study three systems: Si, Mg, and MgO.

Comparison of the SFs to all-electron DFT has shown that it is capable of achieving all-electron accuracy if an all-electron augmentation charge is used for both norm-conserving and ultrasoft pseudopotentials. Further comparisons to experimental SFs has highlighted the ability of this approach to understand the deficiencies in the different DFAs of DFT. In particular, we have found that the differences in frozen core density, often considered unimportant, provide a non-negligible contribution to the SF accuracy of the DFA.

We note that whilst this work has focused on simple solids, the computational efficiency afforded by the developed approach allows for the treatment of larger systems than ever before, such as proteins, defects, surfaces, or molecular crystals and large porous systems. Additionally, its implementation into a PP DFT code means that these systems can be studied with more sophisticated functionals as well.

[1] C. R. Groom, I. J. Bruno, M. P. Lightfoot, and S. C. Ward, Acta Cryst. B **72**, 171 (2016).

[2] H. M. Berman, J. Westbrook, Z. Feng, G. Gilliland, T. N. Bhat, H. Weissig, I. N. Shindyalov, and P. E. Bourne, Nucl. Acids Res. **28**, 235 (2000).

[3] C. Hammond, *The Basics of Crystallography and Diffraction*, International Union of Crystallography Texts on Crystallography, 4th ed. (Oxford University Press, Oxford, 2015).

[4] P. Hohenberg and W. Kohn, Phys. Rev. **136**, B864 (1964).

[5] P. N. H. Nakashima, A. E. Smith, J. Etheridge, and B. C. Muddle, Science **331**, 1583 (2011).

[6] J. M. Zuo, M. Kim, M. O'Keeffe, and J. C. H. Spence, Nature (London) **401**, 49 (1999).

[7] E. M. Forgan, E. Blackburn, A. T. Holmes, A. K. R. Briffa, J. Chang, L. Bouchenoire, S. D. Brown, R. Liang, D. Bonn, W. N. Hardy, N. B. Christensen, M. V. Zimmermann, M. Hücker, and S. M. Hayden, Nat. Commun. **6**, 10064 (2015).

[8] H. Mori, S. Lee, A. Yamamoto, S. Tajima, and S. Sato, Phys. Rev. B **65**, 092507 (2002).

[9] E. Aubert, S. Lebègue, M. Marsman, T. T. T. Bui, C. Jelsch, S. Dahaoui, E. Espinosa, and J. G. Ángyán, J. Phys. Chem. A **115**, 14484 (2011).

[10] W. Jauch and M. Reehuis, Acta Cryst. A **61**, c422 (2005).

[11] W. Jauch and M. Reehuis, Phys. Rev. B **80**, 125126 (2009).

[12] W. Jauch and M. Reehuis, Phys. Rev. B **83**, 115102 (2011).

[13] S. Shibata, F. Hirota, and T. Shioda, J. Mol. Struct. **485-486**, 1 (1999).

[14] J. M. Zuo, M. O'Keeffe, P. Rez, and J. C. H. Spence, Phys. Rev. Lett. **78**, 4777 (1997).

[15] Y. Ogata, K. Tsuda, and M. Tanaka, Acta Cryst. A **64**, 587 (2008).

[16] D. Peng and P. N. H. Nakashima, Phys. Rev. Lett. **126**, 176402 (2021).

[17] L. Wu, Y. Zhu, T. Vogt, H. Su, J. W. Davenport, and J. Tafto, Phys. Rev. B **69**, 064501 (2004).

[18] G. Taylor, Acta Cryst. D **59**, 1881 (2003).

[19] C. J. Howard and R. D. G. Jones, Acta Cryst. A **33**, 776 (1977).

[20] M. C. Schmidt, R. Colella, and D. R. Yoder-Short, Acta Cryst. A **41**, 171 (1985).

[21] M. S. Schmøkel, L. Bjerg, F. K. Larsen, J. Overgaard, S. Cenedese, M. Christensen, G. K. H. Madsen, C. Gatti, E. Nishibori, K. Sugimoto, M. Takata, and B. B. Iversen, Acta Cryst. A **69**, 570 (2013).

[22] D. Peng and P. N. H. Nakashima, J. Appl. Cryst. **50**, 602 (2017).

[23] T. Gruene and E. Mugnaioli, Chem. Rev. **121**, 11823 (2021).

[24] J. M. Zuo, P. Blaha, and K. Schwarz, J. Phys.: Condens. Matter **9**, 7541 (1997).

[25] J. Friis, G. K. H. Madsen, F. K. Larsen, B. Jiang, K. Marthinsen, and R. Holmestad, J. Chem. Phys. **119**, 11359 (2003).

[26] R. Sæterli, E. Flage-Larsen, J. Friis, O. M. Løvvik, J. Pacaud, K. Marthinsen, and R. Holmestad, Ultramicroscopy **111**, 847 (2011).

[27] M. Bursch, J.-M. Mewes, A. Hansen, and S. Grimme, Angew. Chem. Int. Ed. Engl. **61**, e202205735 (2022).

[28] M. G. Medvedev, I. S. Bushmarinov, J. Sun, J. P. Perdew, and K. A. Lyssenko, Science **355**, 49 (2017).

[29] J. Aarons, M. Sarwar, D. Thompsett, and C.-K. Skylaris, J. Chem. Phys. **145**, 220901 (2016).

[30] P. Schwerdtfeger, ChemPhysChem **12**, 3143 (2011).

[31] P. E. Blöchl, Phys. Rev. B **50**, 17953 (1994).

[32] G. Kresse and D. Joubert, Phys. Rev. B **59**, 1758 (1999).

[33] C. Audouze, F. Jollet, M. Torrent, and X. Gonze, Phys. Rev. B **73**, 235101 (2006).

[34] A. Dal Corso, Phys. Rev. B **81**, 075123 (2010).

[35] B. Adolph, J. Furthmüller, and F. Bechstedt, Phys. Rev. B **63**, 125108 (2001).

[36] M. Gajdoš, K. Hummer, G. Kresse, J. Furthmüller, and F. Bechstedt, Phys. Rev. B **73**, 045112 (2006).

[37] J. Yan, J. J. Mortensen, K. W. Jacobsen, and K. S. Thygesen, Phys. Rev. B **83**, 245122 (2011).

[38] J. Vinson, J. J. Rehr, J. J. Kas, and E. L. Shirley, Phys. Rev. B **83**, 115106 (2011).

[39] C. J. Pickard and F. Mauri, Phys. Rev. B **63**, 245101 (2001).

[40] J. R. Yates, C. J. Pickard, and F. Mauri, Phys. Rev. B **76**, 024401 (2007).

[41] M. Taillefumier, D. Cabaret, A.-M. Flank, and F. Mauri, Phys. Rev. B **66**, 195107 (2002).

[42] O. Bunău and M. Calandra, Phys. Rev. B **87**, 205105 (2013).

[43] M. Unzog, A. Tal, and G. Kresse, Phys. Rev. B **106**, 155133 (2022).

[44] E. Flage-Larsen, O. M. Løvvik, Ø. Prytz, and J. Taftø, Comput. Mater. Sci. **47**, 752 (2010).

[45] D. Vanderbilt, Phys. Rev. B **41**, 7892 (1990).

[46] D. D. Koelling and B. N. Harmon, J. Phys. C: Solid State Phys. **10**, 3107 (1977).

[47] B. Hetényi, F. De Angelis, P. Giannozzi, and R. Car, J. Chem. Phys. **115**, 5791 (2001).

[48] K. Laasonen, A. Pasquarello, R. Car, C. Lee, and D. Vanderbilt, Phys. Rev. B **47**, 10142 (1993).

[49] K. Lejaeghere, G. Bihlmayer, T. Björkman, P. Blaha, S. Blügel, V. Blum, D. Caliste, I. E. Castelli, S. J. Clark, A. D. Corso, S. de Gironcoli, T. Deutsch, J. K. Dewhurst, I. D. Marco, C. Draxl, M. Dułak, O. Eriksson, J. A. Flores-Livas, K. F. Garrity, L. Genovese *et al.*, Science **351**, aad3000 (2016).

[50] See Supplemental Material at http://link.aps.org/supplemental/10.1103/PhysRevB.108.115112 for computational details, pseudopotential information, a description of the Hirshfeld partitioning scheme for applying Debye-Waller factors and more detailed structure factor comparisons between different materials, DFT functionals, and pseudopotential approximations; G. Kresse and J. Furthmüller, Comput. Mater. Sci. **6**, 15 (1996).

[51] *International Tables for Crystallography. Vol. B: Reciprocal Space*, 2nd ed., edited by U. Shmueli (Kluwer Academic, Dordrecht, 2001).

[52] S. J. Clark, M. D. Segall, C. J. Pickard, P. J. Hasnip, M. I. J. Probert, K. Refson, and M. C. Payne, Z. Kristallogr. **220**, 567 (2005).

[53] P. Blaha, K. Schwarz, F. Tran, R. Laskowski, G. K. H. Madsen, and L. D. Marks, J. Chem. Phys. **152**, 074101 (2020).

[54] S. R. Jensen, S. Saha, J. A. Flores-Livas, W. Huhn, V. Blum, S. Goedecker, and L. Frediani, J. Phys. Chem. Lett. **8**, 1449 (2017).

[55] P. Wind, M. Bjørgve, A. Brakestad, G. A. Gerez S., S. R. Jensen, R. D. R. Eikås, and L. Frediani, J. Chem. Theory Comput. **19** 137 (2022).

[56] R. J. Harrison, G. Beylkin, F. A. Bischoff, J. A. Calvin, G. I. Fann, J. Fosso-Tande, D. Galindo, J. R. Hammond, R. Hartman-Baker, J. C. Hill, J. Jia, J. S. Kottmann, M.-J. Yvonne Ou, J. Pei, L. E. Ratcliff, M. G. Reuter, A. C. Richie-Halford, N. A. Romero, H. Sekino, W. A. Shelton *et al.*, SIAM J. Sci. Comput. **38**, S123 (2016).

[57] P. Coppens, *X-Ray Charge Densities and Chemical Bonding*, International Union of Crystallography Texts on Crystallography No. 4 (International Union of Crystallography, New York, 1997).

[58] W. H. Bragg, Proc. Phys. Soc. London **33**, 304 (1920).

[59] J. L. Lawrence, Acta Cryst. A **29**, 94 (1973).

[60] V. Valvoda and J. Jeńný, Phys. Status Solidi A **44**, 557 (1977).

[61] C. Malica and A. Dal Corso, Acta Cryst. A **75**, 624 (2019).

[62] S. L. Dudarev, L.-M. Peng, S. Y. Savrasov, and J.-M. Zuo, Phys. Rev. B **61**, 2506 (2000).

[63] F. L. Hirshfeld, Theoret. Chim. Acta **44**, 129 (1977).

[64] J. Yang, L. Z. Tan, and A. M. Rappe, Phys. Rev. B **97**, 085130 (2018).

[65] J. Madsen, T. J. Pennycook, and T. Susi, Ultramicroscopy, **231**, 113253 (2021).

[66] J. M. Zuo, Rep. Prog. Phys. **67**, 2053 (2004).

[67] S. Borghardt, F. Winkler, Z. Zanolli, M. J. Verstraete, J. Barthel, A. H. Tavabi, R. E. Dunin-Borkowski, and B. E. Kardynal, Phys. Rev. Lett. **118**, 086101 (2017).

[68] T. Naginey, Applications of Electronic Structure Theory in Electron Microscopy, Ph.D. thesis, University of Oxford (2018).

[69] G. T. Martinez, T. C. Naginey, L. Jones, C. M. O'Leary, T. J. Pennycook, R. J. Nicholls, J. R. Yates, and P. D. Nellist, arXiv:1907.12974.

[70] T. Susi, J. Madsen, U. Ludacka, J. J. Mortensen, T. J. Pennycook, Z. Lee, J. Kotakoski, U. Kaiser, and J. C. Meyer, Ultramicroscopy **197**, 16 (2019).

[71] C. Hofer, J. Madsen, T. Susi, and T. J. Pennycook, arXiv:2301.04469.

[72] E. J. Kirkland, *Advanced Computing in Electron Microscopy*, 2nd ed. (Springer US, New York, 2010).

[73] Github, https://github.com/benshi97/Data_XRD_Structure_Factor.

[74] Colab, https://colab.research.google.com/github/benshi97/Data_XRD_Structure_Factor/blob/main/analyse.ipynb.